Open Access Library Journal
2026, Volume 13, e15773
ISSN Online: 2333-9721
ISSN Print: 2333-9705

Multiscale Sea Level Variability, Surface Geostrophic Circulation and Mesoscale Eddy Dynamics in the Tropical Western Indian Ocean: Insights from Satellite Altimetry (1993-2024)

Karen Kutsuru[1], John W. Makokha[1], Geoffrey W. Khamala[2]

[1]Department of Science, Technology and Engineering, Kibabii University, Bungoma, Kenya
[2]Department of Renewable Energy and Technology, Turkana University College, Lodwar, Kenya
Email: makokhajw@kibu.ac.ke

How to cite this paper: Kutsuru, K., Makokha, J.W. and Khamala, G.W. (2026) Multiscale Sea Level Variability, Surface Geostrophic Circulation and Mesoscale Eddy Dynamics in the Tropical Western Indian Ocean: Insights from Satellite Altimetry (1993-2024). *Open Access Library Journal*, **13**: e15773.
https://doi.org/10.4236/oalib.1115773

Received: July 16, 2026
Accepted: September 20, 2026
Published: September 23, 2026

Abstract

The Western Indian Ocean (WIO) is one of the most dynamically active ocean regions globally, yet its multiscale interactions and collective influence on sea level variability, surface circulation, and mesoscale eddy activity remain unquantified across the full satellite altimetry era despite direct effect on regional climate prediction, coastal adaptation, and marine ecosystem management along the East African coastline. This study presents an integrated analysis across the tropical WIO (40˚E - 52˚E, 20˚S - 12˚N) using a 32-year satellite altimetry record (1993-2024), employing seasonal decomposition, linear regression with autocorrelation-adjusted significance testing, a non-parametric trend test, and Pearson and partial correlation analysis. Seasonal SLA patterns reveal a monsoon-driven annual cycle characterized by the strongest positive anomalies during MAM, a pronounced cross-equatorial dipole during JJA, and a localized negative coastal anomaly during SON unique to that season. Domain-averaged seasonal SLA exhibits significant positive trends of 3.54 - 4.17 mm yr^{-1}, with an annual mean trend of 3.81 mm yr^{-1} exceeding the global rate of 3.3 - 3.4 mm yr^{-1}. Both El Niño-Southern Oscillation (ENSO) and Indian Ocean Dipole (IOD) significantly modulate WIO sea level during DJF, while ENSO remains significant when controlling for IOD during MAM as IOD remains significant when controlling ENSO during SON while neither index is significant during JJA. Surface geostrophic circulation confirms the monsoon-driven Somali Current reversal and the year-round persistence SEC-EACC western boundary current system. While decrease in mesoscale eddy activity has been reported for many tropical ocean regions, the tropical WIO exhibits significant EKE intensification across all seasons, highlighting the distinctive dynamics of this boundary-current-dominated region. SON is more energetic than MAM across circulation and EKE, while MAM exhibits the strongest positive SLA signal of the annual cycle. These findings advance understanding of WIO multiscale ocean dynamics, providing an observational baseline for regional climate prediction and early warning systems in the region.

Subject Areas

Physical Oceanography, Climate Science, Remote Sensing

Keywords

Sea Level Anomaly, Surface Geostrophic Circulation, Eddy Kinetic Energy, Tropical Western Indian Ocean, Satellite Altimetry

1. Introduction

The Western Indian Ocean (WIO) stands as one of the most dynamic and climatically sensitive marine regions globally [1] [2]. It plays a critical role in regulating regional climate patterns, monsoon rainfall [3], productivity in marine ecosystem [4]-[6], and the coastal sea level along the East African coast, which is heavily populated [7]. It also displays a complex spectrum of climate variability across intraseasonal to decadal periodicities, the majority of which exhibit intrinsic coupling with the basin's distinct seasonal monsoon cycle [1] [2]. The WIO has also been warming more rapidly than any other tropical ocean basin over the last century, significantly impacting Indian Ocean Dipole (IOD) dynamics, East African rainfall patterns, and marine ecosystem health [2] [8]-[11].

The region is defined by a unique seasonal reversal of surface circulation driven by the Indian Ocean monsoon system [1] [12], a characteristic that fundamentally distinguishes it from other tropical ocean basins. This monsoon-driven forcing results in significant seasonal fluctuations in western boundary current intensity, most notably the Somali Current, which reverses direction twice a year in direct response to alternating southwest and northeast monsoon winds [1] [13].

The mesoscale eddy field in the Western Indian Ocean (WIO) has been partially mapped by global census studies [14]. Furthermore, regional research has detailed the seasonal evolution and interannual variability of the Somali Current and Great Whirl system [15]-[17], as well as the dynamic eddy activity within the Mozambique Channel [18] [19]. Earlier research has established the seasonal cycle of Western Indian Ocean sea level anomalies [12] [20] and broader sea level variability across the Indian Ocean [21] [22]. Further studies have also examined the interannual modulation of Indian Ocean sea levels by ENSO and the IOD [23] [24], as well as the long-term positive sea level trend linked to warming in the region [25] [26].

Despite the existing research, there are still considerable gaps in our comprehension of WIO variability. Most studies usually focus on specific aspects of WIO dynamics such as seasonal sea level fluctuations, interannual variability, or mesoscale eddy characteristics individually. As a result, comprehensive multiscale investigations simultaneously examining sea level anomalies, surface geostrophic circulation, and eddy kinetic energy encompassing the entire satellite altimetry period remain limited. Second, although tropical-scale analyses indicate an overall decline in mesoscale variability [27], whether this behavior extends to the boundary-current-dominated tropical western Indian Ocean still remains unclear. Thirdly, the seasonal dependence of ENSO and IOD teleconnections with sea level across the tropical western Indian Ocean has not been comprehensively quantified across the extensive altimetry record. Fourth, although individual studies have noted an asymmetry between the two inter-monsoon transition periods, this phenomenon has not been documented across multiple ocean variables as a coherent, multivariable feature of tropical WIO dynamics.

This research tackles existing gaps by performing an extensive examination of 32 years of satellite altimetry data from 1993 to 2024 in the tropical WIO (40˚E - 52˚E, 20˚S - 12˚N). Specifically, the goals of this study are to: 1) describe the seasonal average patterns and variations of sea level anomalies (SLA) in the tropical WIO and their relationship to monsoon dynamics; 2) assess long-term seasonal SLA trends and analyze how they are influenced by ENSO and the IOD through correlation analysis; 3) outline the climatological average and seasonal surface geostrophic circulation along with its monsoon-induced variability; and 4) evaluate the seasonal patterns and long-term changes in mesoscale eddy kinetic energy across the region. Collectively, these analyses provide a multiscale dynamical characterization of tropical WIO, enhancing the understanding of regional ocean variability and its sensitivity to monsoon forcing and large-scale climate modes.

2. Data and Methodology

2.1. Study Area

The geographical scope of this study covers the tropical WIO region (40˚E - 52˚E, 20˚S - 12˚N), encompassing the East African Coastal Current (EACC) system, the Somali Current system and its associated Great Whirl eddy, the westward propagating South Equatorial Current (SEC) and its characteristic bifurcation along the East Africa margin, and the equatorial WIO where Kelvin wave dynamics exert a significant influence on regional sea level variability. The domain is bounded to the north by the Gulf of Aden and the Arabian Peninsula and includes the Mozambique Channel between the African mainland and Madagascar in the southern portion. The western boundary is delineated by the East African coastline, encompassing the coastal areas of Kenya, Tanzania, Mozambique, and Somalia. These regions are characterized by elevated socioeconomic vulnerability to sea level rise (see **Figure 1**).

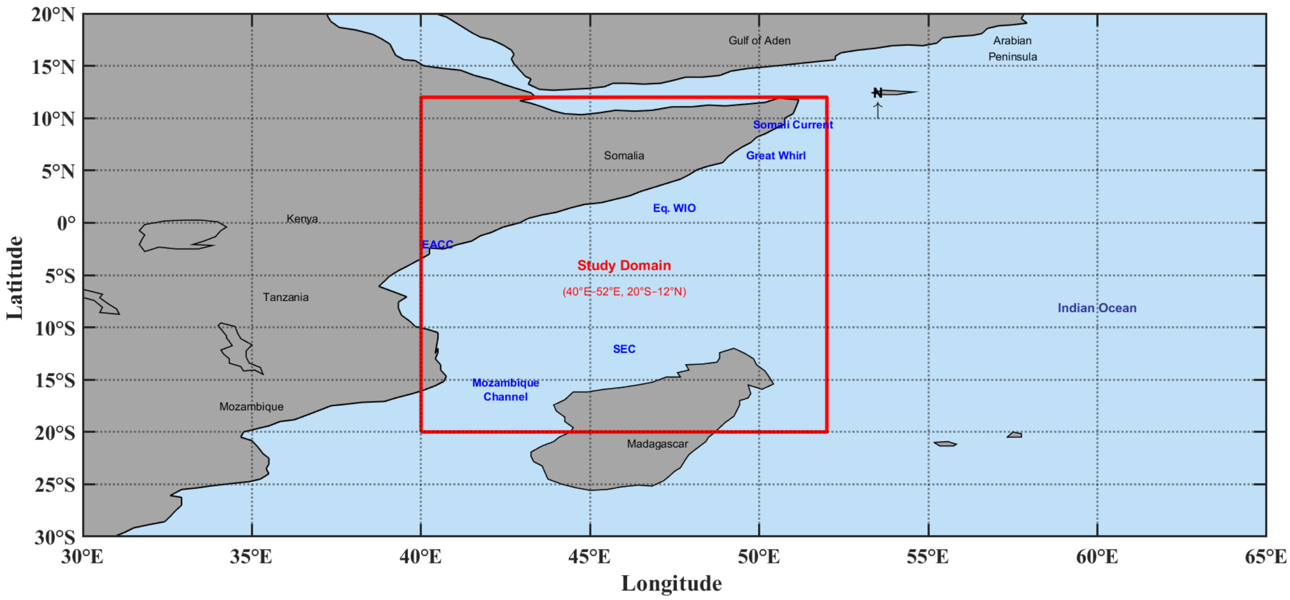

Figure 1. Study area map of the tropical Western Indian Ocean (WIO) showing the study domain (40˚E - 52˚E, 20˚S - 12˚N) delineated by the red box. Key oceanographic features within and surrounding the domain are labelled, including the EACC, Somali Current, Great Whirl, SEC, and the equatorial WIO (Eq. WIO). The Gulf of Aden and Arabian Peninsula are shown for broader regional context, while the Mozambique Channel and Madagascar, a key secondary mesoscale eddy region examined in this study, are labelled for their analytical relevance. Gray shading denotes land.

2.2. Data

Satellite-derived sea level anomaly and surface geostrophic velocity data were obtained from the Copernicus Marine Environment Monitoring Service (CMEMS) multi-year reprocessed merged multi mission gridded altimetry dataset (https://data.marine.copernicus.eu/product/SEALEVEL_GLO_PHY_L4_MY_008_047/download?dataset=cmems_obs-sl_glo_phy-ssh_my_allsat-14-duacs-0.25deg_P1M-m), based on merged multi-mission satellite altimetry observations dis tributed on a regular 0.125˚ × 0.125˚ geographic grid.

Monthly mean SLA fields were obtained from the product cmems_obs-sl_glo_phy-ssh_my_allsat-l4-duacs-0.125deg_P1M-m, ranging from January 1993 to December 2024. Daily surface geostrophic velocity components eastward (ugos) and northward (vgos) were extracted from the product cmems_obs-sl_glo_phy-ssh_my_allsat-l4-duacs-0.125deg_P1D over the same period. Both products are derived from the DUACS DT2018 reprocessing system [28], which integrates observations from multiple satellite altimeters to ensure consistent and homogeneous sea level and geostrophic velocity fields throughout the altimetry era.

To characterize climate variability, the Niño3.4 index, serving as a proxy for the El Niño-Southern Oscillation (ENSO), was derived from the National Oceanic and Atmospheric Administration (NOAA) Climate Prediction Center (CPC) Extended Reconstructed Sea Surface Temperature version 5 (ERSSTv5) dataset. The Dipole Mode Index (DMI), representing Indian Ocean Dipole (IOD) dynamics, was obtained from the NOAA Physical Sciences Laboratory. Data for both indices were acquired for the 1993-2024 period and subsequently processed into seasonal averages aligned with the four standard meteorological seasons.

Prior to analysis, both datasets were spatially constrained to the defined study domain (40˚E - 52˚E, 20˚S - 12˚N). To ensure statistical integrity, grid cells containing missing data were systematically excluded from spatial averaging via the omitnan function in MATLAB R2018b, thereby restricting domain-averaged metrics to valid oceanic grid points.

2.3. Methodology

2.3.1. Seasonal Decomposition

Monthly SLA fields were temporally aggregated into four distinct meteorological seasons: DJF, MAM, JJA, and SON, corresponding to the Northeast monsoon, first inter-monsoon, Southwest monsoon, and second inter-monsoon periods, respectively. Seasonal mean SLA patterns were derived by averaging all available monthly data for each season throughout the 1993-2024 period. The variability of seasonal SLA was assessed by calculating the STD of monthly SLA for each grid point within each season. Daily geostrophic velocity components ugos and vgos were processed into seasonal means by averaging all available daily data within each season across the entire 1993-2024 record; this approach bypassed intermediate monthly averaging to maximize the retention of high-frequency temporal variability within the seasonal mean flow fields.

The surface geostrophic current speed was computed as:

$$U = \sqrt{\mathrm{ugos}^2 + \mathrm{vgos}^2} \quad (1)$$

Where U represents the magnitude of the seasonal mean geostrophic flow vector. The method ensures that directional cancellation between opposing flow components is preserved in the seasonal mean, so that U (Equation (1)) reflects the true magnitude of the time-averaged circulation rather than the mean of instantaneous speeds. For visual clarity, velocity vectors were spatially subsampled at every tenth grid point.

2.3.2. Trend Analysis

Domain-averaged seasonal SLA time series were calculated by spatially averaging SLA throughout the entire study area for each season and each year. Linear trends were determined using ordinary least squares (OLS) regression.

$$\mathrm{SLA}_t = \beta_0 + \beta_1 t + \varepsilon_t \quad (2)$$

where β_1 is the linear trend and ε_t the regression residuals with significance assessed using a two-tailed Student's t-test applied to the regression slope [29]. Since temporal autocorrelation can inflate apparent significance of a detected Trend [30], the lag-1 autocorrelation of the residuals, r_1 was computed for each season and the effective sample size calculated according to [31].

$$N_{eff} = n \cdot \left(\frac{1 - r_1}{1 + r_1} \right) \quad (3)$$

The statistical significance of all trends was evaluated through the Trend-Free Pre-Whitened Modified Mann-Kendall (TFPW-MK) test with Sen's slope estimation [30] applied. The trend was first estimated using [32] slope, the median of all pairwise slopes

$$\beta_{Sen} = \text{median}\left(\frac{y_j - y_i}{x_j - x_i}\right) \tag{4}$$

where y_j and x_i are paired observations with $i < j$.

Trend magnitudes are expressed in mm yr^{-1} alongside 95% confidence intervals. The coefficient of determination (R^2) was calculated for each seasonal regression to quantify the proportion of variance accounted for by the linear trend. To maintain temporal consistency across all seasonal time series, the domain-averaged SLA record was trimmed to the 1993-2024 period, with the partial DJF 2025 season, consisting solely of December 2024, was omitted from the trend analysis to prevent bias from an incomplete seasonal mean.

2.3.3. Interannual Variability and Climate Mode Analysis

To isolate interannual SLA variability from the secular trend, a linear detrending procedure was applied to each seasonal SLA time series prior to correlation analysis. Pearson correlation coefficients were calculated between the detrended seasonal SLA anomalies and the concurrent seasonal Niño3.4 and DMI values at zero lag [33]. Statistical significance for these coefficients was determined via a two-tailed t-test with $n - 2 = 30$ degrees of freedom and a sample size of $n = 32$. Subsequently, a lagged correlation analysis was conducted for intervals ranging from 0 to 6 seasons where positive lags denote the climate index preceding the SLA response to evaluate potential delayed atmospheric and oceanic forcing from ENSO and IOD on regional sea levels. Statistical significance for all correlation coefficients was evaluated at the 95% and 99% confidence intervals. Since multiple lagged correlations were evaluated, these analyses were treated as explatory and interpreted cautiously. The full results are provided in (Supplementary **Table A1**).

Since ENSO and IOD can co-vary, partial correlations were additionally computed for each season, assessing each index's relationship with SLA while statistically controlling for the other:

$$r_{\text{SLA,ENSO}\cdot\text{IOD}} = \frac{r_{\text{SLA,ENSO}} - r_{\text{SLA,IOD}} \cdot r_{\text{ENSO,IOD}}}{\sqrt{\left(1 - r_{\text{SLA,IOD}}^2\right)\left(1 - r_{\text{ENSO,IOD}}^2\right)}} \tag{5}$$

with the equivalent expression for IOD controlling for ENSO, allowing each index's independent contribution to be isolated from claims based on pairwise correlations alone. All computational analyses were executed using MATLAB R2018b (MathWorks, Natick, MA, USA).

2.3.4. Eddy Kinetic Energy Computation

Surface eddy kinetic energy (EKE) was quantified from the daily geostrophic zonal (u) and meridional (v) velocities obtained from CMEMS gridded altimetry product, following [14] [34] standard formulation used in altimetry based EKE studies.

Daily velocity fields were used since temporal averaging prior to computing velocity anomalies would smooth out and underestimate genuine sub-monthly eddy variability [14]. To isolate transient mesoscale variability from predictable seasonal cycle of the underlying current system, climatological monthly mean was adopted [35]. Monthly climatological geostrophic velocity fields were computed for each calendar month by averaging all daily geostrophic velocity fields belonging to the same calendar month over the 1993-2024 study period.

$$\bar{u}(x,y,m)=\frac{1}{N_m}\sum_{i=1}^{N_m}u(x,y,m,i),\bar{v}(x,y,m)=\frac{1}{N_m}\sum_{i=1}^{N_m}v(x,y,m,i) \tag{6}$$

where $\bar{u}(x,y,m)$ and $\bar{v}(x,y,m)$ are the climatological zonal and meridional geostrophic velocities for calendar month m at grid location (x,y), N_m is the total number of daily observations available for month m, and i represents all daily observations belonging to that calendar month. Daily geostrophic velocity anomalies were obtained by subtracting the corresponding monthly climatological velocity from each daily field:

$$u'(x,y,t)=u(x,y,t)-\bar{u}(x,y,m),v'(x,y,t)=v(x,y,t)-\bar{v}(x,y,m) \tag{7}$$

while the daily eddy kinetic energy was then computed at each grid point before seasonal averaging, in order to fully capture the temporal variability of the mesoscale eddy field:

$$\mathrm{EKE}(x,y,t)=0.5\times\left[u'^2(x,y,t)+v'^2(x,y,t)\right] \tag{8}$$

Monthly climatological velocity was removed to suppress the recurring seasonal circulation while preserving transient departures from the climatological state, so that the resulting EKE fields primarily represent mesoscale eddy variability rather than seasonal fluctuations of the background circulation.

Seasonal mean EKE fields were obtained by averaging all daily EKE values within each climatological season (DJF, MAM, JJA, SON):

$$\overline{\mathrm{EKE}}_s(x,y)=\frac{1}{n_s}\sum_{j=1}^{n_s}\mathrm{EKE}(x,y,j) \tag{9}$$

To assess the basin-wide interannual variability in mesoscale eddy activity, domain-averaged seasonal EKE time series were obtained by spatially averaging the seasonal mean EKE for each year. Seasonal domain-mean EKE was calculated as an unweighted spatial average across all grid cells within the study domain, given the low-latitude extent of the study domain (20˚S - 12˚N), this was considered appropriate, and a comparison against a cosine-latitude-weighted domain mean showed differences of less than 1% across all seasons, confirming that area weighting does not materially affect the reported results. The interannual trends in seasonal domain-mean EKE were assessed using the same procedure applied to SLA trends (Section 2.3.2); ordinary least squares regression with an effective-sample-size correction for autocorrelation [31], cross-validated using the Trend-Free Pre-Whitened Modified Mann-Kendall test with Sen's slope estimation [30].

3. Results and Discussion

3.1. Seasonal Mean Sea Level Anomaly Patterns and Monsoon Driven Control

The spatial distribution of seasonal mean SLA throughout the tropical WIO displays significant variability, governed by the monsoon cycle (**Figure 2**), reflecting the dominant influence of monsoon forcing on surface dynamics of WIO [1] [12] [36]. During the NE monsoon DJF, positive SLA anomalies prevail in the domain with stronger values along the Somali coast at approximately 10˚N - 11˚N and the SEC band (15˚S to 10˚S), while a localized negative anomaly is identified further offshore (4˚N - 7˚N), distinct from the coastal positive signal while weaker positive anomalies characterize the southern EACC and equatorial region. The increased signal in Somali coast suggests reversal to downwelling-favorable Ekman transport under the weak, southward-flowing NE monsoon Somali Current, in contrast to the upwelling-favorable conditions of the SW monsoon [12].

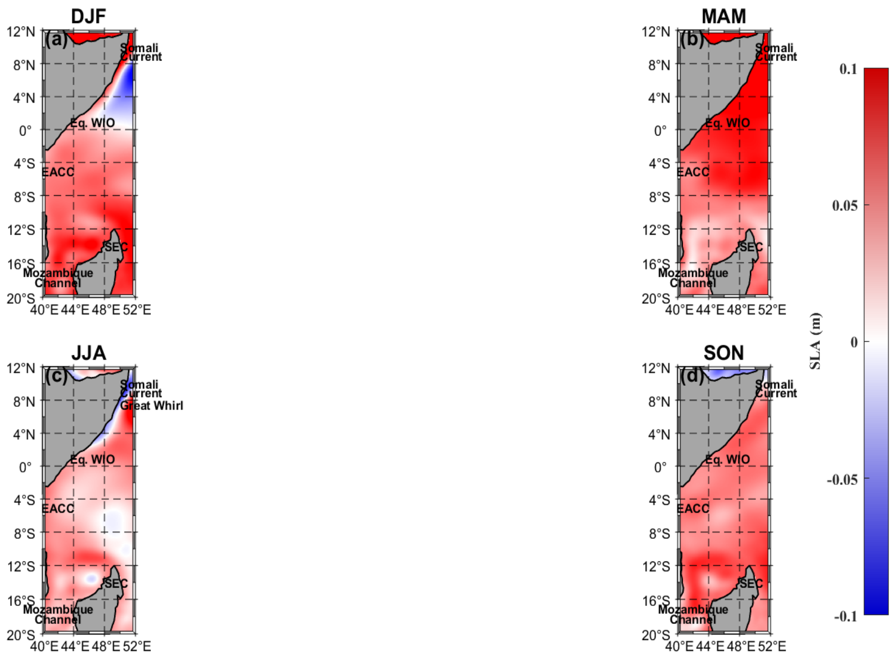

Figure 2. Seasonal mean sea level anomaly (SLA, m) patterns across the tropical Western Indian Ocean for (a) December-February (DJF), (b) March-May (MAM), (c) June-August (JJA), and (d) September-November (SON), derived from satellite altimetry data for the period 1993-2024. Positive (negative) values indicate above (below) normal sea level relative to the 1993-2024 mean. Key circulation features are labelled. Gray shading denotes land.

Strongest positive SLA anomalies is characterized during the first inter-monsoon period (MAM), especially in the northern domain with no negative subregions, probably linked to the seasonal buildup of upper-ocean heat prior to the southwest monsoon, which is consistent with the documented pattern of pre-monsoon warming followed by rapid cooling of the Arabian Sea warm pool in the adjacent northwestern Indian Ocean [37]. The southwest monsoon (JJA) shows the weakest SLA pattern across most of the domain with a localized negative anomaly near the Somali coast (9˚N - 10˚N), which marks the beginning of intense coastal upwelling driven by the Somali Jet. This process, coupled with Ekman-driven offshore transport, shoals the thermocline and reflects the formation of the Great Whirl under the established southwest monsoon [38] [39]. The southern EACC maintains moderate positive anomalies largely independent of the southwest monsoon upwelling system. During the second intermonsoon (SON), positive SLA persists across the equatorial and southern domains, but a localised negative anomaly emerges along the northern Somali coast at 11˚N to 12˚N, a location that remains strongly positive during both DJF and MAM, at a distinct latitude from the JJA negative signature further south. This pattern is consistent with residual coastal upwelling from the retreating SW monsoon Somali Jet continuing into the early autumn transition, ahead of the current's full reversal to its NE monsoon mode [13]. MAM exhibits the strongest positive SLA of the annual cycle, coinciding with the pre-monsoon warming period of the northwestern Indian Ocean reported in previous studies [37]. SON maintains a residual upwelling effect from the prior SW Monsoon, which delays the full re-establishment of positive SLA along the Somali coast.

3.2. Seasonal SLA Variability and Its Dynamical Drivers

The tropical WIO exhibits spatially heterogeneous patterns, as evidenced by seasonal SLA variability, which is expressed as the standard deviation of monthly SLA within each season (**Figure 3**). The DJF displays the highest domain-wide variability, characterized by enhanced STD along the EACC and extending into the equatorial WIO which is consistent with the robust, simultaneous modulation of WIO sea levels by the ENSO and IOD, as established in Section 3.3. MAM exhibits comparable variability along the EACC corridor but is more limited to the western boundary, showing weaker variability in the equatorial WIO compared to DJF. JJA is marked by a pronounced intensification of variability in the northern domain, coinciding with the development of the Great Whirl and Somali Current mesoscale activity [39], while EACC variability is the weakest of all which suggests the local monsoon forcing dominance over the remote interannual climate modes during the SW monsoon. SON pattern is comparable to JJA in the northern domain surpassing MAM which confirms an inter-monsoon asymmetry that remains constrained to the northern domain rather than reflecting as a basin-wide pattern. This is consistent with the continued presence of Somali Current and Great Whirl mesoscale activity into the early autumn transition prior to the full current reversal. The pronounced maximum variability is observed near the Mozambique Channel and the coast of Madagascar throughout all seasons, which is consistent to the region's well-documented persistent mesoscale eddy field [40].

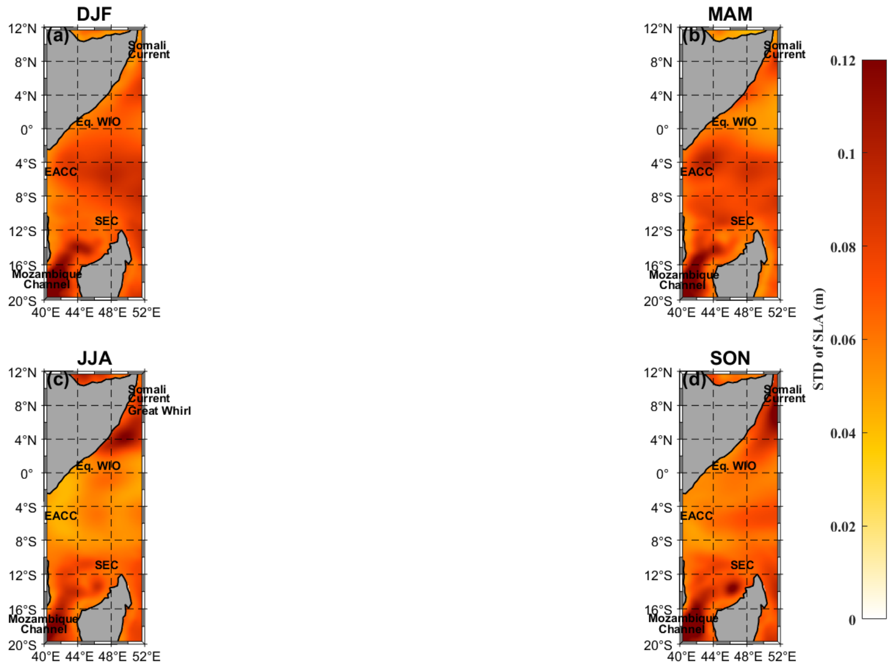

Figure 3. Spatial distribution of seasonal sea level anomaly (SLA) variability, expressed as the standard deviation (STD, m) of monthly SLA, for (a) December-February (DJF), (b) March-May (MAM), (c) June-August (JJA), and (d) September-November (SON), derived from satellite altimetry data over the period 1993-2024. Gray shading denotes land.

3.3. Interannual Sea Level Anomaly Trends and Climate Mode Modulation

Averaged interannual seasonal SLA time series for the tropical WIO shows a consistent positive rise across all seasons from 1993 to 2024 (Figure 4). Linear trends for DJF, MAM, JJA, and SON are 3.54, 3.89, 3.62, and 4.17 mm yr^{-1}, (Sen's slope: 3.26, 3.73, 3.38, and 4.14 mm yr^{-1}) respectively, with corresponding 95% CI of 1.93 - 5.16, 2.54 - 5.24, 2.76 - 4.49, and 3.10 - 5.23 mm yr, consistent with established satellite altimetry research on Indian Ocean sea level rise [26]. JJA and SON exhibited modest positive autocorrelation (r_1 = 0.28 and 0.23, respectively), reducing the effective sample size to approximately 18 and 20 (from n = 32), while DJF and MAM showed negligible autocorrelation (r_1 = −0.04 and −0.02). All seasonal trends remained highly significant ($p < 0.01$) after applying the effective sample size correction of [31], and this robustness was independently confirmed using the Trend-Free Pre-Whitened Modified Mann-Kendall test with Sen's slope estimation [30] which yielded Z-statistics of 4.14 to 4.62 ($p < 0.001$) across all seasons.

The annual mean domain-averaged SLA trend of 3.81 mm yr^{-1} surpasses the global mean rate of approximately 3.3 - 3.4 mm yr^{-1} [41] [42]. This suggests an intensified regional sea level rise in the tropical WIO, substantiating prior evidence of sea level acceleration in the Indian Ocean [26] [43] [44]. SON exhibits the most significant long-term secular trend (4.17 mm yr^{-1}), consistent with the synergistic effect of thermosteric sea-level rise and positive SLA signatures associated with the IOD, which preferentially intensify sea level during the boreal autumn [24] [45] [46]. JJA season accounts for the greatest proportion of variance explained by the linear trend ($R^2 = 0.71$), and the maximal Mann-Kendall Z-score (5.47), confirming the most monotonic upward trend, characterized by minimal interannual interference.

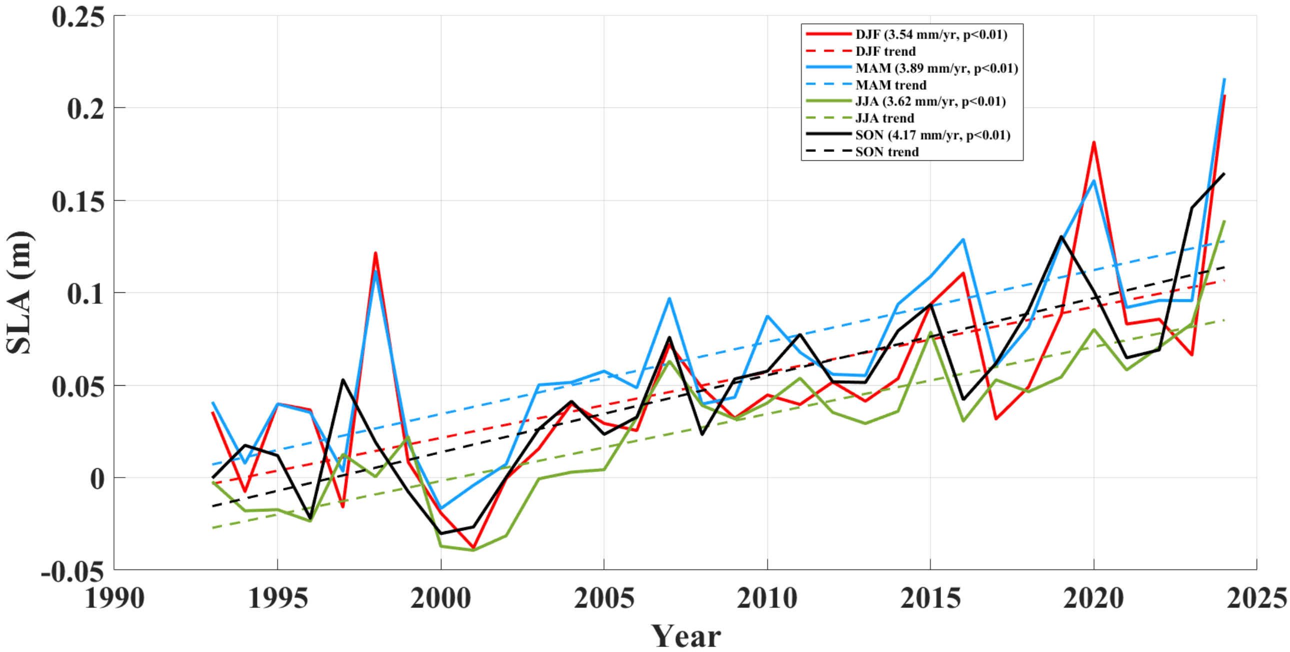

Figure 4. Interannual seasonal sea level anomaly (SLA, m) time series averaged over the tropical Western Indian Ocean for DJF (red), MAM (blue), JJA (black), and SON (green) during 1993-2024, derived from satellite altimetry data. Dashed lines denote linear trend fits for each season with rates and significance levels indicated in the legend. All trends are statistically significant ($p < 0.01$) after effective-sample-size correction for temporal autocorrelation independently confirmed by the Trend-Free Pre-Whitened Modified Mann-Kendall test with Sen's slope estimation.

In contrast, DJF shows the lowest R^2 (0.40), indicating the high amplitude interannual variability, associated with ENSO and monsoonal dynamics, partially masks the underlying secular trend. Correlation analysis between detrended seasonal SLA anomalies and the Niño3.4 and DMI indices shows that the influence of these climate modes on WIO sea level variability fluctuates seasonally throughout the 1993-2024 period, as shown in **Table 1**. There are significant positive correlations with both Niño3.4 ($r = 0.65$, $p < 0.01$) and DMI ($r = 0.72$, $p < 0.01$) during DJF which demonstrates a delayed oceanic reaction to the preceding ENSO and IOD peaks in SON transmitted via equatorial Kelvin waves and thermocline depth anomalies [23] [24]. Partial correlation analysis confirms both relationships remain significant when controlling for the other index with the stronger IOD correlation consistent with the study area's proximity to the IOD's western pole, which drives the most significant SLA signatures in the WIO [46]. A significant correlation exists in MAM with Niño3.4 ($r = 0.64$), but not with DMI ($r = 0.06$). This ENSO relationship remains fully significant after controlling for IOD, consistent with El Nino driven basin-wide warming across the Indian Ocean via atmospheric teleconnections [47] [48]. During JJA, neither Niño3.4 nor the DMI exhibits a statistically significant correlation with detrended SLA at the 95% confidence level. The lack of significant ENSO or IOD correlation during JJA aligns with the physical dominance of local Southwest monsoon forcing, which overwhelms remote interannual [1] [39]. Contrarily, during SON, significant zero-order correlations with both indices are observed Niño3.4 (r = 0.36) and the DMI (r = 0.51). However, due to the strong covariance between ENSO and the IOD during this season, partial correlation analysis reveals that only the IOD relationship remains significant when ENSO is controlled for confirming the IOD's dominant independent role in modulating WIO sea levels at the peak of its development during the boreal autumn [23] [24]. The apparent ENSO correlation reflects its covariance with IOD rather than an independent physical mechanism.

Table 1. Pearson correlation coefficients (r) between detrended seasonal SLA anomalies and the Niño3.4 index (ENSO) and Dipole Mode Index (DMI, IOD) over the tropical Western Indian Ocean for the period 1993-2024. Significance levels: ***$p < 0.01$, **$p < 0.05$, ns = not significant.

Season	r (Niño3.4)	p	r (DMI)	p
DJF	0.65	<0.01***	0.72	<0.01***
MAM	0.64	<0.01 ***	0.06	0.75 ns
JJA	0.05	0.79 ns	0.32	0.08 ns
SON	0.36	<0.05**	0.51	<0.01***

Note: Partial correlation analysis (Section 3.3) shows that the SON Niño3.4 correlation does not remain significant when controlling for IOD, indicating this relationship reflects covariance between the two indices rather than an independent ENSO influence.

3.4. Seasonal Surface Geostrophic Circulation

Seasonal mean surface geostrophic circulation patterns in the tropical Western Indian Ocean, calculated from ugos and vgos components, demonstrate a significant monsoon-driven annual system characterized by seasonal reversal of the Somali current between its southward NE monsoon mode during DJF and its northward SW monsoon mode from MAM through SON (**Figure 5**). This monsoon is confined to the Somali Current rather than the boundary current system as a whole, corresponding with previous observational and modeling research [12] [20]. The EACC and SEC emerge as prominent year-round circulation features, with the EACC appearing as a strong northward coastal jet along the East African coast and the SEC as a persistent westward band at approximately 10˚S - 15˚S, bifurcating at the East African coast into northward EACC flow and southward flow toward the Mozambique Channel. Their persistence to maintain their unidirectional flow throughout the year, though their strength varies seasonally, marks them as stable components of tropical WIO circulation, in contrast to Somali's current genuine directional reversal.

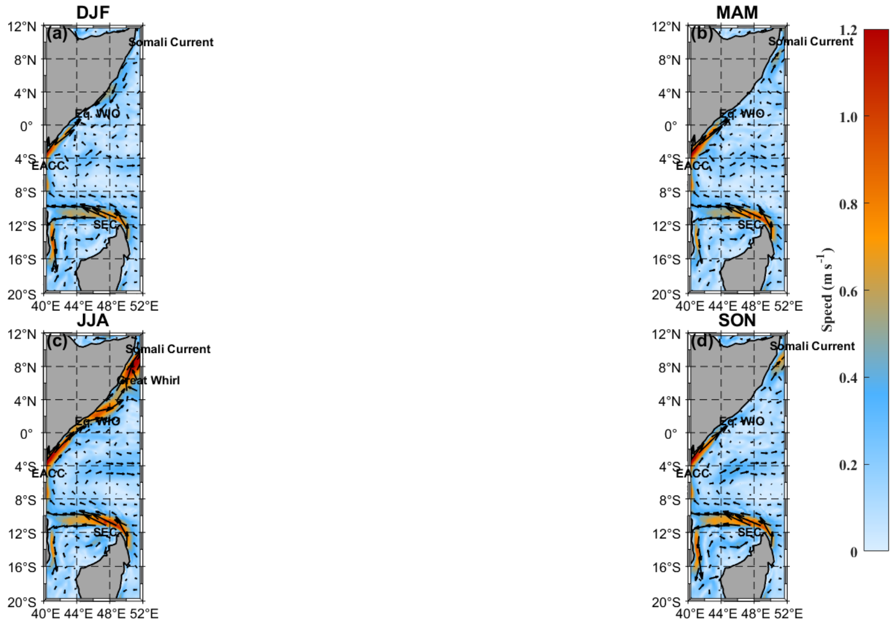

Figure 5. Seasonal mean surface geostrophic circulation across the tropical WIO for (a) December-February (DJF), (b) March-May (MAM), (c) June-August (JJA), and (d) September-November (SON), derived from satellite altimetry-based ugos and vgos components for the period 1993-2024. Color shading represents current speed (m s^{-1}) with warm colors (orange red) indicating high speeds associated with strong boundary currents and cool colors (blue, white) indicating weak equatorial flow. Arrows indicate flow direction and speed subsampled at every tenth grid point for clarity. Key circulation features are labelled. Gray shading denotes land.

The EACC weakens during DJF, then intensifies progressively through MAM and JJA before declining again in SON, demonstrating how the SEC-driven western boundary current system persists throughout the year independent of the state of low-level Somali Jet, which triggers intense northeastward Ekman transport and sustains the geostrophic flow associated with this anticyclonic eddy [12] [16] [38], then weakens through SON toward its DJF state. The Somali Current and Great Whirl maintains elevated speeds onto SON, surpassing MAM levels. This reflects the gradual weakening of the SW monsoon Somali Jet, rather than an abrupt reversal. The pattern mirrors the inter-monsoon asymmetry found in northern regions for SLA variability in section 3.2. Throughout the domain, SON exhibits systematically stronger flow than MAM across the Somali Current, Great Whirl region, SEC, and basin-wide mean while EACC is the exception, whereby MAM speeds exceed SON. The observed EACC maintains a year-round northward flow, with seasonal intensity controlled by SEC transport contributions and sea level gradients that propagate remotely as Rossby waves from the southwest Indian Ocean [49] [50]; however, this interpretation should be considered in light of the increased uncertainty associated with gridded altimetry-derived geostrophic velocities in coastal regions. This mechanism accounts for its unique seasonal timing, which differs from the Somali Current-driven asymmetry observed elsewhere in the domain.

3.5. Climatological Mean Circulation and Boundary Current Structure

The climatological average surface geostrophic circulation, based on the comprehensive satellite altimetry data from 1993 to 2024, depicts prevailing mean flow state of the WIO (**Figure 6**), shows substantial congruence with established characterizations of the WIO mean flow field [12] The East African Coastal Current emerges as the key climatological circulation characteristic, manifesting as a strong northward coastal jet along the East African shoreline approximately 2˚S - 5˚S, with maximum speeds of 1.24 m s^{-1}, which is the most sustained speeds within the mean field. This is consistent with the documented year round persistence as a northward western boundary current sustained by the SEC bifurcation regardless of monsoon phase [49]. The SEC forms a coherent westward-flowing band, attaining its peak climatological speed at approximately 10.8˚S before reaching the East African coast, where it bifurcates into the northward-flowing EACC and a southward branch feeding the Mozambique Channel at approximately 10.6˚S.

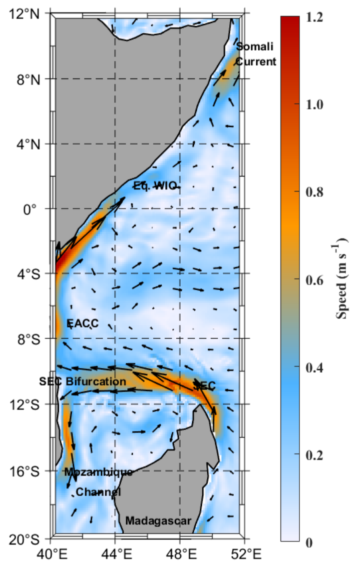

Figure 6. Climatological mean surface geostrophic circulation derived from satellite altimetry over the period 1993-2024 across the tropical WIO. Color shading represents mean current speed (m s^{-1}) computed from the magnitude of the climatological mean ugos and vgos components, with warm colors (orange red) indicating strong boundary current flow and cool colors (light blue, white) indicating weak equatorial and open-ocean interior flow away from the boundary currents. Arrows indicate mean flow direction subsampled at every tenth grid point for clarity. Key circulation features are labelled. Gray shading denotes land.

This bifurcation latitude is consistent with observational studies indicating that the Northeast Madagascar Current reaches the East African coast near 11˚S, where the flow subsequently turns northward to form the EACC [51]-[53]. The northern domain which includes the Somali Current system at 5˚N and 12˚N exhibits relatively weak climatological mean speeds of 0.40 m s^{-1}, with a northward vector tendency reflecting the partial dominance of the stronger SW monsoon northward flow over the weaker NE monsoon southward flow in the long-term mean. The equatorial interior exhibits near neutral weak flow, consistent with the seasonal asymmetry described in Section 4.4. The near neutral equatorial mean flow reflects the partial cancellation of seasonal reversal of the equatorial jets as evidenced by the weak and mixed direction vectors observed in this region. The equatorial interior exhibits weak, near-neutral flow, reflecting the partial cancellation of seasonally reversing equatorial jets over the annual cycle.

3.6. Seasonal Eddy Kinetic Energy Distribution

Analysis of the seasonal mean EKE across the tropical WIO demonstrates significant spatial heterogeneity in mesoscale eddy dynamics, modulated by monsoon cycle (Figure 7), consistent with the preferential formation of mesoscale eddies along western boundary currents and major current systems, a pattern that corresponds with global EKE observations [14]. Enhanced EKE is concentrated along the Somali Current system north of the equator during JJA and SON, consistent with previous studies attributing enhanced mesoscale eddy activity in the region to baroclinic and barotropic instabilities associated with the intense horizontal velocity shear inherent to western boundary currents [1] [39], while EKE along the EACC corridor remains comparatively modest throughout the annual cycle.

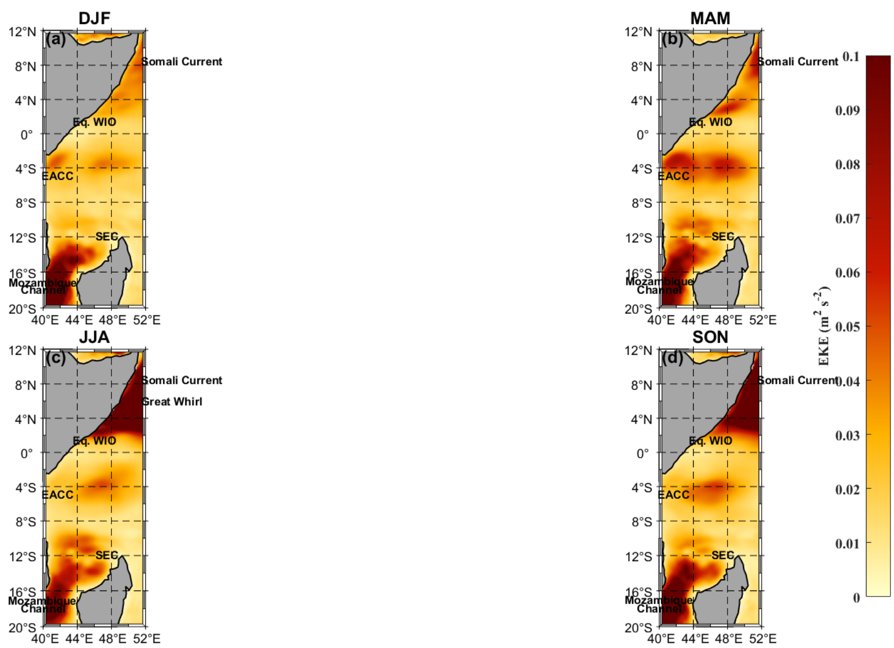

Figure 7. Seasonal mean eddy kinetic energy (EKE, $m^2 s^{-2}$) across the tropical WIO for (a) December-February (DJF), (b) March-May (MAM), (c) June-August (JJA), and (d) September-November (SON), computed as $EKE = \frac{1}{2}\left(u'^2 + v'^2\right)$ where u' and v' are geostrophic velocity anomalies relative to the 1993-2024 climatological mean. The color bar is capped at 0.10 $m^2 s^{-2}$ to highlight basin-wide spatial patterns; maximum values reaching 0.27 $m^2 s^{-2}$ –0.30 $m^2 s^{-2}$ during JJA, SON are associated with intense mesoscale eddy activity in the Somali Current and Great Whirl region, while the domain wide maximum during DJF and MAM occurs in the southern Mozambique Channel/Madagascar region. Gray shading denotes land.

The domain mean EKE for DJF, MAM, JJA, and SON are 0.0285, 0.0317, 0.0391, and 0.0417 $m^2 s^{-2}$, respectively, with SON having the highest domain-wide mean and DJF the lowest. Within the Somali Current/Great Whirl region, JJA remains the most energetic season, exceeding SON, consistent with the established seasonal peak of Great Whirl formation during the SW monsoon [39]. The higher domain-wide EKE in SON relative to JJA does not reflect stronger boundary-current activity during SON, but rather the Mozambique Channel/Madagascar region where EKE is comparable to or exceeds the Somali Current/Great Whirl region during DJF, MAM and especially SON. Excluding the Mozambique Channel brings JJA and SON EKE into near parity, indicating that the domain-wide reversal results from two seasonally out-of-phase regions rather than primarily reflecting a weakening of JJA boundary-current activity. This pattern in the Mozambique Channel is presented as an observation rather than a mechanistically explained result, as existing literature on eddy seasonality in the region reports mixed and contrasting cycles depending on the sub-regional location [54]. A domain-wide EKE maximum also occurs in this southern region during DJF and, to a lesser extent MAM, however, regional means provide a more robust basis for comparison because single grid-cell maxima are sensitive to localized variability. Peak EKE values of 0.30 $m^2 s^{-2}$ occur within the Somali Current and Great Whirl region during JJA, and SON. In **Figure 7**, the color bar is capped at 0.10 $m^2 s^{-2}$ to better highlight on the basin-wide spatial patterns.

3.7. Long-Term EKE Trends and Basin-Wide Intensification

Analysis of domain-averaged seasonal eddy EKE time series from 1993 to 2024 demonstrates a statistically significant positive trajectory across all seasons, suggesting a basin-wide intensification of mesoscale eddy activity within the tropical WIO (**Figure 8**) during the satellite altimetry era. This finding contrasts with the general decline reported for the tropical ocean by [27]; instead, it corresponds with their documented increase of 2% - 5% per decade in mesoscale variability within eddy-active boundary current regions, which is consistent with the WIO Somali current and Great Whirl system rather than the broader tropical ocean average. Calculated trends for DJF, MAM, JJA, and SON are 2.55×10^{-4}, 3.56×10^{-4}, 4.70×10^{-4}, and 3.46×10^{-4} $m^2 s^{-2} yr^{-1}$, respectively. Lag-1 autocorrelation was weak in DJF ($r_1 = 0.02$) but more pronounced in SON ($r_1 = 0.21$), reducing the effective sample size in SON to approximately 21, whereas MAM and JJA exhibited no meaningful autocorrelation. All the trends remained statistically significant after applying the effective sample size correction of [31], with MAM and JJA significant at $p < 0.01$ and DJF and SON at $p < 0.05$, independently confirmed by the Trend-Free Pre-Whitened Modified Mann-Kendall test [30] (Z = 2.74 - 4.07, $p < 0.01$ for all seasons); Sen's slope estimates closely matched the OLS trends throughout. JJA exhibits the strongest EKE trend and highest variance explained ($R^2 = 0.468$), whereas DJF shows the weakest trend and lowest variance explained ($R^2 = 0.190$), indicating greater interannual variability relative to the trend in this season. The JJA trend strength is consistent with the dominant role of the southwest monsoon in driving Somali Current and Great Whirl intensification through the same mechanism identified for the seasonal circulation patterns in this study [38] [39].

The increasing EKE trends are physically consistent with the concurrent positive SLA trends in Section 3.3. Increased sea level gradients align with enhanced geostrophic current shear along the western boundary and may provide favorable conditions for increased mesoscale eddy activity through processes such as baroclinic instability [55]-[57]. However, since the present analysis is based solely on satellite altimetry-derived sea level and geostrophic velocities, these mechanisms are inferred rather than directly demonstrated.

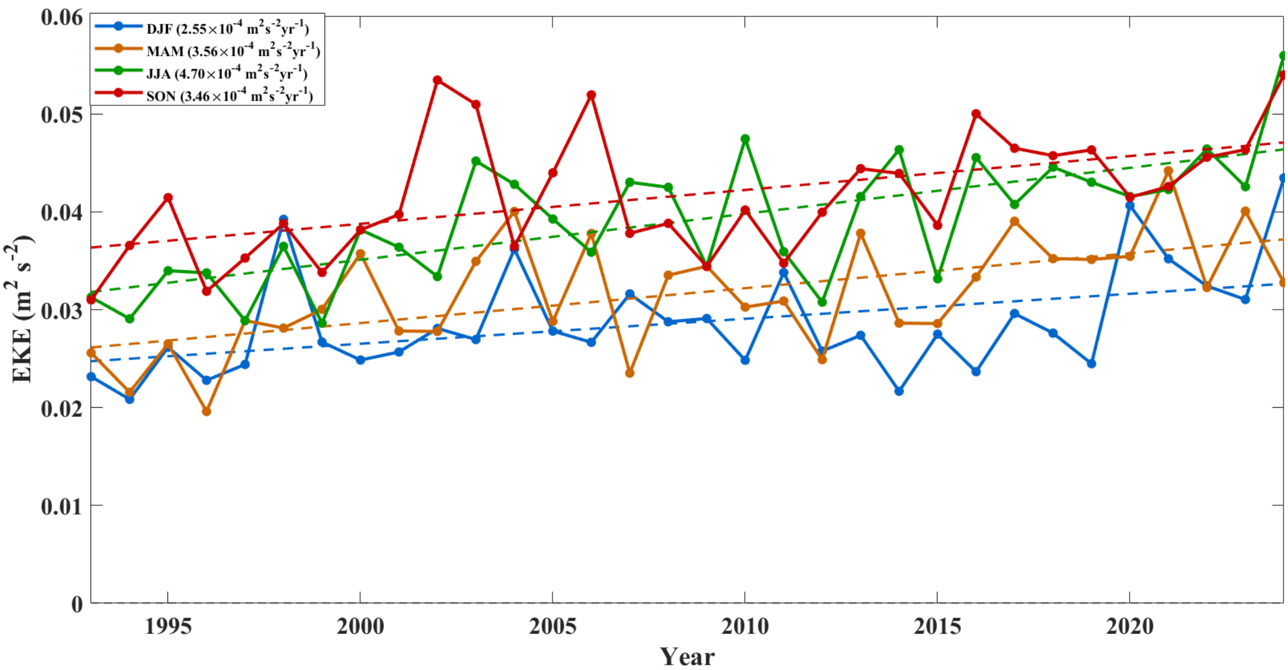

Figure 8. Interannual seasonal eddy kinetic energy (EKE, $m^2\ s^{-2}$) time series averaged over the tropical Western Indian Ocean for DJF (blue), MAM (orange), JJA (green), and SON (red) during 1993-2024. Dashed lines denote linear trend fits for each season with rates indicated in the legend. All trends are statistically significant after effective-sample-size correction for temporal autocorrelation ($p < 0.001$ for MAM and JJA, $p < 0.05$ for DJF and SON), independently confirmed by the Trend-Free Pre-Whitened Modified Mann-Kendall test with Sen's slope estimation.

3.8. Study Limitations

The interpretations presented in this study are based on satellite altimetry-derived sea level and geostrophic velocities. Consequently, the analyses do not directly resolve subsurface temperature, density structure, wind forcing, or the dynamical processes responsible for mesoscale eddy generation, such as baroclinic instability. Therefore, interpretations linking the observed SLA and EKE variability to mechanisms including thermosteric expansion, changes in geostrophic current shear, or baroclinic instability should be regarded as physically plausible explanations supported by previous studies rather than directly demonstrated mechanisms. In addition, gridded altimetry-derived geostrophic velocities are subject to greater uncertainty in coastal regions and narrow passages since the underlying sea level fields are themselves known to be less reliable within approximately 10 - 15 km of the coast due to land masking and reduced accuracy of geophysical corrections [58]. Accordingly, interpretations of circulation and EKE associated with the East African Coastal Current, the SEC bifurcation, and the Mozambique Channel should be considered within these observational limitations.

4. Conclusion

This study provides a comprehensive multiscale analysis of sea level anomaly (SLA) variability, surface geostrophic circulation, and mesoscale eddy kinetic energy (EKE) across the tropical WIO. The seasonal cycle of WIO dynamics exhibits asymmetry, with MAM exhibiting the highest positive SLA, coinciding with the pre-monsoon warming preceding the onset of the SW monsoon. During JJA, spatial contrast is robust through the superposition of intense Somali Jet-driven coastal upwelling in the north and persistent positive anomalies maintained by the EACC in the south. Furthermore, the identification of undocumented localized negative SLA along the northern Somali coast during SON implies that residual upwelling conditions from the retreating SW monsoon retard the complete re-establishment of positive sea level. Domain-averaged seasonal (SLA) shows significant positive trends of 3.54 - 4.17 mm yr^{-1} across all seasons ($p < 0.01$). The corresponding annual mean trend of 3.81 mm yr^{-1} surpasses the global mean of approximately 3.3 - 3.4 mm yr^{-1}, indicating an increasing regional sea level. Correlation analysis reveals a distinct seasonal dependence on climate mode teleconnections. ENSO and IOD jointly modulate WIO sea levels during DJF, while partial correlation analysis confirms that only IOD exerts an independent influence during SON once ENSO's covariance with IOD is accounted for. ENSO is the dominant driver during MAM, while both indices have negligible influence during JJA, as local southwest monsoon forcing decouples the regional ocean from remote teleconnections. Surface geostrophic circulation shows that monsoon forcing exerts its dominant influence through the Somali Current, the only boundary current in the domain to undergo a genuine seasonal reversal, whereas the EACC and the SEC constitute a consistent year-round western boundary current system, whose strength rather than direction responds to monsoon phases. During the inter-monsoon period, SON displays more energy than MAM across circulation and EKE but is less energetic than MAM in SLA, indicating different physical states, and the variable-dependent asymmetry represents a previously undocumented multivariable characteristic in tropical WIO dynamics. Mesoscale eddy activity is strongly regulated by monsoon-driven boundary current instability, with the Somali Current and Great Whirl system representing the dominant EKE source during JJA and SON and the Mozambique Channel eddy field constituting a persistent secondary source of comparable or greater magnitude during DJF and MAM. DJF records the lowest domain mean EKE of the annual cycle, while both

DJF and MAM exhibit domain-wide EKE peaks in the southern Madagascar region rather than in the north, indicating a significant reorganization of mesoscale eddy activity outside the JJA/SON boundary current dominant period. Statistical analysis, validated through effective-sample-size-adjusted parametric testing and an independent non-parametric test, reveals significant positive EKE trends ranging from 2.55 - 4.70 × 10^{-4} m^2 s^{-2} yr^{-1} across all seasons, highlighting an intensification of mesoscale eddy activity that, in contrast to reported declines across the broader tropical ocean, positions the tropical WIO as an eddy-rich exception within a tropical setting. These results have significant implications for regional climate forecasting, early warning systems, and coastal adaptation strategies along the East African coast, where sea-level fluctuations driven by the IOD and ENSO impact flood risks, fishery yields, and marine ecosystems. Future research should integrate subsurface observations from Argo floats and mooring arrays to directly test thermosteric, wind-driven, and baroclinic instability mechanisms rather than relying on altimetry-derived proxies alone. Additionally, utilizing higher-resolution coupled ocean-atmosphere models will be essential to examine the mechanistic connections between Indian Ocean warming, potential boundary currents, and mesoscale eddy energy over multi-decadal timescales.

Data Availability Statement

The satellite altimetry sea level anomaly data and the surface geostrophic velocity data, (cmems_obs-sl_glo_phy-ssh_my_allsat-l4-duacs-0.125deg_P1M-m) (cmems_obs-sl_glo_phy-ssh_my_allsat-l4-duacs-0.125deg_P1D), both part of the SEALEVEL_GLO_PHY_L4_MY_008_047 dataset, are freely available from the Copernicus Marine Environment Monitoring Service (CMEMS) at https://marine.copernicus.eu. The Niño3.4 index was obtained from the NOAA Climate Prediction Center at https://www.cpc.ncep.noaa.gov, while the DMI was obtained from the NOAA Physical Sciences Laboratory at https://psl.noaa.gov.

Author Contributions

Conceptualization, [KK] and [MJW]; methodology, [KK]; software, [KK]; validation, [KK] and [KGW]; formal analysis, [KK]; investigation, [KK]; resources, [KK], [MJW] and [KGW]; data curation, [KK]; writing—original draft preparation, [KK]; writing—review and editing, [KK] and [KGW]; visualization, [KK]; supervision, [MJW]; project administration, [MJW]. All authors have read and agreed to the published version of the manuscript.

Conflicts of Interest

The authors declare no conflict of interest pertaining to the publication of this paper.

References

[1] Schott, F.A., Xie, S.P. and McCreary Jr., J.P. (2009) Indian Ocean Circulation and Climate Variability. *Reviews of Geophysics*, **47**, RG1002.

https://doi.org/10.1029/2007rg000245

[2] Roxy, M.K., Ritika, K., Terray, P. and Masson, S. (2014) The Curious Case of Indian Ocean Warming. *Journal of Climate*, **27**, 8501-8509. https://doi.org/10.1175/jcli-d-14-00471.1

[3] Black, E., Slingo, J. and Sperber, K.R. (2003) An Observational Study of the Relationship between Excessively Strong Short Rains in Coastal East Africa and Indian Ocean SST. *Monthly Weather Review*, **131**, 74-94. https://doi.org/10.1175/1520-0493(2003)131<0074:aosotr>2.0.co;2

[4] Lévy, M., Shankar, D., André, J.M., Shenoi, S.S.C., Durand, F. and de Boyer Montégut, C. (2007) Basin-Wide Seasonal Evolution of the Indian Ocean's Phytoplankton Blooms. *Journal of Geophysical Research*: *Oceans*, **112**, C12014. https://doi.org/10.1029/2007jc004090

[5] Roxy, M.K., Modi, A., Murtugudde, R., Valsala, V., Panickal, S., Prasanna Kumar, S., *et al.* (2016) A Reduction in Marine Primary Productivity Driven by Rapid Warming over the Tropical Indian Ocean. *Geophysical Research Letters*, **43**, 826-833. https://doi.org/10.1002/2015gl066979

[6] Dalpadado, P., Roxy, M.K., Arrigo, K.R., van Dijken, G.L., Chierici, M., Ostrowski, M., *et al.* (2024) Rapid Climate Change Alters the Environment and Biological Production of the Indian Ocean. *Science of the Total Environment*, **906**, Article ID: 167342. https://doi.org/10.1016/j.scitotenv.2023.167342

[7] Ballesteros, C. and Esteves, L.S. (2021) Integrated Assessment of Coastal Exposure and Social Vulnerability to Coastal Hazards in East Africa. *Estuaries and Coasts*, **44**, 2056-2072. https://doi.org/10.1007/s12237-021-00930-5

[8] Joseph, L., Dey, D., Skliris, N., Sanchez-Franks, A., Marsh, R., Hirschi, J., *et al.* (2025) Warming Trend in the Western Indian Ocean Driven by Oceanic Transport. *Journal of Geophysical Research*: *Oceans*, **131**, e2025JC022762. https://doi.org/10.1029/2025jc022762

[9] Nicholson, S.E. (2017) Climate and Climatic Variability of Rainfall over Eastern Africa. *Reviews of Geophysics*, **55**, 590-635. https://doi.org/10.1002/2016rg000544

[10] Jacobs, Z.L., Yool, A., Jebri, F., Srokosz, M., van Gennip, S., Kelly, S.J., *et al.* (2021) Key Climate Change Stressors of Marine Ecosystems along the Path of the East African Coastal Current. *Ocean & Coastal Management*, **208**, Article ID: 105627. https://doi.org/10.1016/j.ocecoaman.2021.105627

[11] Roxy, M.K., Gnanaseelan, C., Parekh, A., Chowdary, J.S., Singh, S., Modi, A., *et al.* (2020) Indian Ocean Warming. In: Krishnan, R., Sanjay, J., Gnanaseelan, C., Mujumdar, M., Kulkarni, A. and Chakraborty, S., Eds., *Assessment of Climate Change over the Indian Region*, Springer Singapore, 191-206. https://doi.org/10.1007/978-981-15-4327-2_10

[12] Schott, F.A. and McCreary, J.P. (2001) The Monsoon Circulation of the Indian Ocean. *Progress in Oceanography*, **51**, 1-123. https://doi.org/10.1016/s0079-6611(01)00083-0

[13] Wang, H., McClean, J.L., Talley, L.D. and Yeager, S. (2018) Seasonal Cycle and Annual Reversal of the Somali Current in an Eddy-Resolving Global Ocean Model. *Journal of Geophysical Research*: *Oceans*, **123**, 6562-6580. https://doi.org/10.1029/2018jc013975

[14] Chelton, D.B., Schlax, M.G. and Samelson, R.M. (2011) Global Observations of Nonlinear Mesoscale Eddies. *Progress in Oceanography*, **91**, 167-216. https://doi.org/10.1016/j.pocean.2011.01.002

[15] Schott, F., Fischer, J., Garternicht, U. and Quadfasel, D. (1997) Summer Monsoon

Response of the Northern Somali Current, 1995. *Geophysical Research Letters*, **24**, 2565-2568. https://doi.org/10.1029/97gl00888

[16] Trott, C.B., Subrahmanyam, B. and Murty, V.S.N. (2017) Variability of the Somali Current and Eddies during the Southwest Monsoon Regimes. *Dynamics of Atmospheres and Oceans*, **79**, 43-55. https://doi.org/10.1016/j.dynatmoce.2017.07.002

[17] Trott, C.B., Subrahmanyam, B., Chaigneau, A. and Delcroix, T. (2018) Eddy Tracking in the Northwestern Indian Ocean during Southwest Monsoon Regimes. *Geophysical Research Letters*, **45**, 6594-6603. https://doi.org/10.1029/2018gl078381

[18] Ridderinkhof, H. and de Ruijter, W.P.M. (2003) Moored Current Observations in the Mozambique Channel. *Deep Sea Research Part II: Topical Studies in Oceanography*, **50**, 1933-1955. https://doi.org/10.1016/s0967-0645(03)00041-9

[19] Halo, I., Backeberg, B., Penven, P., Ansorge, I., Reason, C. and Ullgren, J.E. (2014) Eddy Properties in the Mozambique Channel: A Comparison between Observations and Two Numerical Ocean Circulation Models. *Deep Sea Research Part II: Topical Studies in Oceanography*, **100**, 38-53. https://doi.org/10.1016/j.dsr2.2013.10.015

[20] Shankar, D., Vinayachandran, P.N. and Unnikrishnan, A.S. (2002) The Monsoon Currents in the North Indian Ocean. *Progress in Oceanography*, **52**, 63-120. https://doi.org/10.1016/s0079-6611(02)00024-1

[21] Masumoto, Y. and Meyers, G. (1998) Forced Rossby Waves in the Southern Tropical Indian Ocean. *Journal of Geophysical Research: Oceans*, **103**, 27589-27602. https://doi.org/10.1029/98jc02546

[22] Clarke, A.J. and Liu, X. (1994) Interannual Sea Level in the Northern and Eastern Indian Ocean. *Journal of Physical Oceanography*, **24**, 1224-1235. https://doi.org/10.1175/1520-0485(1994)024<1224:islitn>2.0.co;2

[23] Rao, S.A., Behera, S.K., Masumoto, Y. and Yamagata, T. (2002) Interannual Subsurface Variability in the Tropical Indian Ocean with a Special Emphasis on the Indian Ocean Dipole. *Deep Sea Research Part II: Topical Studies in Oceanography*, **49**, 1549-1572. https://doi.org/10.1016/s0967-0645(01)00158-8

[24] Feng, M. and Meyers, G. (2003) Interannual Variability in the Tropical Indian Ocean: A Two-Year Time-Scale of Indian Ocean Dipole. *Deep Sea Research Part II: Topical Studies in Oceanography*, **50**, 2263-2284. https://doi.org/10.1016/s0967-0645(03)00056-0

[25] Church, J.A. and White, N.J. (2011) Sea-Level Rise from the Late 19th to the Early 21st Century. *Surveys in Geophysics*, **32**, 585-602. https://doi.org/10.1007/s10712-011-9119-1

[26] Han, W., Meehl, G.A., Rajagopalan, B., Fasullo, J.T., Hu, A., Lin, J., *et al.* (2010) Patterns of Indian Ocean Sea-Level Change in a Warming Climate. *Nature Geoscience*, **3**, 546-550. https://doi.org/10.1038/ngeo901

[27] Martínez-Moreno, J., Hogg, A.M., England, M.H., Constantinou, N.C., Kiss, A.E. and Morrison, A.K. (2021) Global Changes in Oceanic Mesoscale Currents over the Satellite Altimetry Record. *Nature Climate Change*, **11**, 397-403. https://doi.org/10.1038/s41558-021-01006-9

[28] Taburet, G., Sanchez-Roman, A., Ballarotta, M., Pujol, M., Legeais, J., Fournier, F., *et al.* (2019) DUACS DT2018: 25 Years of Reprocessed Sea Level Altimetry Products. *Ocean Science*, **15**, 1207-1224. https://doi.org/10.5194/os-15-1207-2019

[29] Von Storch, H. and Zwiers, F.W. (2002) Statistical Analysis in Climate Research. Cambridge University Press.

[30] Yue, S. and Wang, C.Y. (2002) Applicability of Prewhitening to Eliminate the Influ-

ence of Serial Correlation on the Mann-Kendall Test. *Water Resources Research*, **38**, 4-1-4-7. https://doi.org/10.1029/2001wr000861

[31] Yue, S. and Wang, C. (2004) The Mann-Kendall Test Modified by Effective Sample Size to Detect Trend in Serially Correlated Hydrological Series. *Water Resources Management*, **18**, 201-218. https://doi.org/10.1023/b:warm.0000043140.61082.60

[32] Sen, P.K. (1968) Estimates of the Regression Coefficient Based on Kendall's Tau. *Journal of the American Statistical Association*, **63**, 1379-1389. https://doi.org/10.1080/01621459.1968.10480934

[33] Cohen, J., Cohen, P., West, S.G. and Aiken, L.S. (2013) Applied Multiple Regression/Correlation Analysis for the Behavioral Sciences. Routledge.

[34] Stammer, D. (1997) Global Characteristics of Ocean Variability Estimated from Regional TOPEX/POSEIDON Altimeter Measurements. *Journal of Physical Oceanography*, **27**, 1743-1769. https://doi.org/10.1175/1520-0485(1997)027<1743:gcoove>2.0.co;2

[35] Rieck, J.K., Böning, C.W., Greatbatch, R.J. and Scheinert, M. (2015) Seasonal Variability of Eddy Kinetic Energy in a Global High-Resolution Ocean Model. *Geophysical Research Letters*, **42**, 9379-9386. https://doi.org/10.1002/2015gl066152

[36] Wyrtki, K. (1973) Physical Oceanography of the Indian Ocean. In: Zeitzschel, B. and Gerlach, S.A., Eds., *The Biology of the Indian Ocean*, Springer, 18-36. https://doi.org/10.1007/978-3-642-65468-8_3

[37] Li, N., Zhu, X., Wang, H., Zhang, S. and Wang, X. (2023) Intraseasonal and Interannual Variability of Sea Temperature in the Arabian Sea Warm Pool. *Ocean Science*, **19**, 1437-1451. https://doi.org/10.5194/os-19-1437-2023

[38] Findlater, J. (1969) A Major Low-Level Air Current near the Indian Ocean during the Northern Summer. *Quarterly Journal of the Royal Meteorological Society*, **95**, 362-380. https://doi.org/10.1002/qj.49709540409

[39] Beal, L.M. and Donohue, K.A. (2013) The Great Whirl: Observations of Its Seasonal Development and Interannual Variability. *Journal of Geophysical Research*: *Oceans*, **118**, 1-13. https://doi.org/10.1029/2012jc008198

[40] Schouten, M.W., de Ruijter, W.P.M., van Leeuwen, P.J. and Ridderinkhof, H. (2003) Eddies and Variability in the Mozambique Channel. *Deep Sea Research Part II*: *Topical Studies in Oceanography*, **50**, 1987-2003. https://doi.org/10.1016/s0967-0645(03)00042-0

[41] Masson-Delmotte, V., Zhai, P., Pirani, A., Connors, S.L., Péan, C., Berger, S., *et al.* (2021) Climate Change 2021: The Physical Science Basis. Contribution of Working Group I to the Sixth Assessment Report of the Intergovernmental Panel on Climate Change. Cambridge University Press, 2391 p.

[42] Nerem, R.S., Beckley, B.D., Fasullo, J.T., Hamlington, B.D., Masters, D. and Mitchum, G.T. (2018) Climate-Change-Driven Accelerated Sea-Level Rise Detected in the Altimeter Era. *Proceedings of the National Academy of Sciences of the United States of America*, **115**, 2022-2025. https://doi.org/10.1073/pnas.1717312115

[43] Cazenave, A. and Cozannet, G.L. (2014) Sea Level Rise and Its Coastal Impacts. *Earth's Future*, **2**, 15-34. https://doi.org/10.1002/2013ef000188

[44] Arias, P., Bellouin, N., Coppola, E., Jones, R., Krinner, G., Marotzke, J., *et al.* (2021) Climate Change 2021: The Physical Science Basis. Contribution of Working Group I to the Sixth Assessment Report of the Intergovernmental Panel on Climate Change; Technical Summary. Cambridge University Press, 33-144.

[45] Wunsch, C., Ponte, R.M. and Heimbach, P. (2007) Decadal Trends in Sea Level Pat-

terns: 1993-2004. *Journal of Climate*, **20**, 5889-5911. https://doi.org/10.1175/2007jcli1840.1

[46] Saji, N.H., Goswami, B.N., Vinayachandran, P.N. and Yamagata, T. (1999) A Dipole Mode in the Tropical Indian Ocean. *Nature*, **401**, 360-363. https://doi.org/10.1038/43854

[47] Du, Y., Xie, S., Huang, G. and Hu, K. (2009) Role of Air-Sea Interaction in the Long Persistence of El Niño-Induced North Indian Ocean Warming. *Journal of Climate*, **22**, 2023-2038. https://doi.org/10.1175/2008jcli2590.1

[48] Xie, S., Hu, K., Hafner, J., Tokinaga, H., Du, Y., Huang, G., *et al.* (2009) Indian Ocean Capacitor Effect on Indo-Western Pacific Climate during the Summer Following El Niño. *Journal of Climate*, **22**, 730-747. https://doi.org/10.1175/2008jcli2544.1

[49] Painter, S.C. (2020) The Biogeochemistry and Oceanography of the East African Coastal Current. *Progress in Oceanography*, **186**, Article ID: 102374. https://doi.org/10.1016/j.pocean.2020.102374

[50] Zheng, C., Zheng, S., Feng, M., Xie, L., Wang, L., Zhang, T., *et al.* (2024) Interannual Variability of the East African Coastal Current Associated with El Niño-Southern Oscillation. *Journal of Climate*, **37**, 4613-4631. https://doi.org/10.1175/jcli-d-23-0563.1

[51] Manyilizu, M., Penven, P. and Reason, C. (2016) Annual Cycle of the Upper-Ocean Circulation and Properties in the Tropical Western Indian Ocean. *African Journal of Marine Science*, **38**, 81-99. https://doi.org/10.2989/1814232x.2016.1158123

[52] Swallow, J.C., Schott, F. and Fieux, M. (1991) Structure and Transport of the East African Coastal Current. *Journal of Geophysical Research: Oceans*, **96**, 22245-22257. https://doi.org/10.1029/91jc01942

[53] Semba, M., Lumpkin, R., Kimirei, I., Shaghude, Y. and Nyandwi, N. (2019) Seasonal and Spatial Variation of Surface Current in the Pemba Channel, Tanzania. *PLOS ONE*, **14**, e0210303. https://doi.org/10.1371/journal.pone.0210303

[54] Bai, L., Zhu, G., Huang, H., Zhang, L., LÜ, H. and Zhang, Y. (2024) Characteristics of Mesoscale Eddies in the Mozambique Channel. *PLOS ONE*, **19**, e0302367. https://doi.org/10.1371/journal.pone.0302367

[55] Gill, A.E., Green, J.S.A. and Simmons, A.J. (1974) Energy Partition in the Large-Scale Ocean Circulation and the Production of Mid-Ocean Eddies. *Deep Sea Research and Oceanographic Abstracts*, **21**, 499-528. https://doi.org/10.1016/0011-7471(74)90010-2

[56] Smith, K.S. (2007) The Geography of Linear Baroclinic Instability in Earth's Oceans. *Journal of Marine Research*, **65**, 655-683. https://doi.org/10.1357/002224007783649484

[57] Pedlosky, J. (2013) Geophysical Fluid Dynamics. 2nd Edition, Springer.

[58] Benveniste, J., Birol, F., Calafat, F., Cazenave, A., Dieng, H., Gouzenes, Y., *et al.* (2020) Coastal Sea Level Anomalies and Associated Trends from Jason Satellite Altimetry over 2002-2018. *Scientific Data*, **7**, Article No. 357. https://doi.org/10.1038/s41597-020-00694-w

Appendix

Table A1. Lag correlations (0 to 6 seasons) between detrended seasonal sea level anomaly (SLA) and the Niño3.4 and Dyad Mode Index (DMI) indices for DJF, MAM, JJA, and SON, 1993-2024. Positive lags indicate the climate index preceding the SLA response. This lag analysis was conducted as an exploratory extension of the zero-lag correlations reported in Table 1 (main text) and, given the substantial number of comparisons involved (7 lags × 2 indices × 4 seasons), any statistically significant lagged correlations should be interpreted with caution and require confirmation in future studies. Lag+0 values correspond exactly to the zero-lag correlations already reported in **Table 1**.

Niño3.4				
Lag	DJF (r, p)	MAM (r, p)	JJA (r, p)	SON (r, p)
0	0.647, 0.0001***	0.641, 0.0001***	0.050, 0.7864	0.356, 0.0456**
+1	0.108, 0.5692	0.394, 0.0284**	0.140, 0.4524	0.320, 0.0789*
+2	−0.227, 0.2353	−0.250, 0.1834	0.197, 0.2969	−0.115, 0.5459
+3	−0.077, 0.6976	−0.109, 0.5741	0.045, 0.8179	−0.148, 0.4431
+4	0.242, 0.2241	0.089, 0.6519	−0.112, 0.5693	−0.091, 0.6456
+5	0.211, 0.2997	0.359, 0.0661*	0.183, 0.3599	0.280, 0.1568
+6	−0.054, 0.7995	−0.148, 0.4700	0.173, 0.3970	0.058, 0.7795
DMI				
Lag	DJF (r, p)	MAM (r, p)	JJA (r, p)	SON (r, p)
0	0.722, 0.0000***	0.058, 0.7520	0.318, 0.0762*	0.513, 0.0027***
+1	0.105, 0.5809	0.188, 0.3109	0.008, 0.9668	0.180, 0.3337
+2	−0.178, 0.3552	−0.320, 0.0851*	−0.203, 0.2822	−0.299, 0.1090
+3	0.011, 0.9562	−0.060, 0.7581	0.019, 0.9207	−0.071, 0.7147
+4	−0.033, 0.8686	0.229, 0.2416	0.051, 0.7947	0.092, 0.6398
+5	0.120, 0.5603	0.187, 0.3507	0.305, 0.1223	0.340, 0.0825*
+6	0.060, 0.7767	−0.055, 0.7900	−0.120, 0.5605	0.053, 0.7980

*p < 0.10; **p < 0.05; ***p < 0.01.